

Elastically-isotropic open-cell minimal surface shell-lattices with superior stiffness via variable thickness design

Qingping Ma ^a, Lei Zhang ^a, Junhao Ding ^b, Shuo Qu ^b, Jin Fu ^c, Mingdong Zhou ^d,
Ming Wang Fu ^c, Xu Song ^b, Michael Yu Wang ^{a,*}

^a *Department of Mechanical and Aerospace Engineering, Hong Kong University of Science and Technology, Kowloon, Hong Kong, China*

^b *Department of Mechanical and Automation Engineering, Chinese University of Hong Kong, Shatin, Hong Kong, China*

^c *Department of Mechanical Engineering, Hong Kong Polytechnic University, Kowloon, Hong Kong, China*

^d *Shanghai Key Laboratory of Digital Manufacture for Thin-walled Structures, School of Mechanical Engineering, Shanghai Jiao Tong University, Shanghai, China*

* Corresponding author: Michael Yu Wang (mywang@ust.hk)

Abstract

Triply periodic minimal surface (TPMS) shell-lattices are attracting increasingly attention due to their unique combination of geometric and mechanical properties, and their open-cell topology. However, uniform thickness TPMS shell-lattices are usually anisotropic in stiffness, namely having different Young's moduli along different lattice directions. To reduce the anisotropy, we propose a family of variable thickness TPMS shell-lattices with isotropic stiffness designed by a strain energy-based optimization algorithm. The optimization results show that all the five selected types of TPMS lattices can be made to achieve isotropic stiffness by varying the shell thickness, among which N14 and OCTO can maintain over 90% of the Hashin-Shtrikman upper bound of bulk modulus. All the optimized shell-lattices exhibit superior stiffness properties and significantly outperform elastically-isotropic truss-lattices. Both uniform and optimized types of N14 shell-lattices along [100], [110] and [111] directions are fabricated by the micro laser powder bed fusion techniques with stainless steel 316L and tested under quasi-static compression loads. Experimental results show that the elastic anisotropy of the optimized N14 lattices is reduced compared to that of the uniform ones. Large deformation compression results reveal different failure deformation behaviors along different directions. The [100] direction shows a layer-by-layer plastic buckling failure mode, while the failures along [110] and [111] directions are related to the shear deformation. The optimized N14 lattices possess a reduced anisotropy of plateau stresses and can even attain nearly isotropic energy absorption capacity.

Keywords: Triply periodic minimal surface; open-cell shell-lattices; isotropic stiffness; laser powder bed fusion; mechanical properties

1. Introduction

Mechanical metamaterials are artificial structures whose mechanical properties are determined by the downscale micro-architectures [1]. By tailoring the architectures, mechanical metamaterials can obtain unconventional mechanical properties unachievable by bulk materials, such as negative Poisson's ratio (auxetics) [2], negative compressibility transitions [3], pentamode materials [4], and maintain high stiffness and strength with low relative densities [1, 5]. Recent advances in additive manufacturing (AM) technologies facilitate the realization of mechanical metamaterials with complex downscale micro-architectures [6, 7].

In recent decades, numerous research efforts have been made to improve the mechanical performance of metamaterials in terms of architecture design. The stochastic foams first appeared as a class of artificial porous elastically-isotropic metamaterials, mainly for energy absorption applications [1, 8]. The subsequent emerging open-cell truss-lattices can outperform stochastic foams of equal relative density in stiffness and strength via the stretching-dominated design concept, and receive considerable attention [9-11]. However, even the optimal stretching-dominated elastically-isotropic truss-lattices can only reach nearly 1/3 of the Hashin-Shtrikman (HS) upper bounds in low relative densities [12-14]. Recent studies have found a family of stretching-dominated elastically-isotropic plate-lattices whose stiffness properties can reach the HS upper bounds in low relative densities [15-17]. However, their closed-cell topology complicates the manufacturing and therefore additional holes need to be added for resin or powder removal in AM process [16-18]. In addition, many applications such as heat exchangers [19], biomedical implants [20, 21] and supercapacitors [22-24] require smooth open channels for mass and heat transfer. Thus, it remains a significant research task to find open-cell metamaterials with superior mechanical properties for multifunctional applications.

Other than stochastic foams, truss-lattices and plate-lattices, shell-lattices provide another opportunity of mechanical metamaterials. They are now attracting increasingly attention for their smooth, periodic and non-intersecting structures to avoid stress concentration and their open-cell topology. The majority of studies on shell-lattices are based on the well-known triply periodic minimal surface (TPMS) [25]. The stiffness and strength of TPMS shell-lattices are proven to exceed those of truss-lattices in a wide range of relative densities [21, 26]. Especially, the bulk moduli of TPMS shell-lattices are numerically confirmed to approach the HS upper bound [27]. Functionally graded designs of TPMS shell-lattices are further developed for enhanced energy absorption capacity [28], exceptional fatigue resistance [29], bone-mimicking transport properties [30], and are widely adopted for tissue engineering scaffolds. Yoo [31] proposed a heterogeneous modeling method to design TPMS scaffolds with controllable porosity, while Vijayavenkataraman et al. [32] further developed a parametric optimization approach for sheet TPMS scaffolds to satisfy multifunctional requirements including stiffness, porosity and pore size.

The studies on shell-lattices above are related to TPMS shell-lattices with uniform thickness, which are usually anisotropic in stiffness – possessing different Young's moduli along different

lattice directions. Several attempts are made to achieve macroscopic isotropic stiffness. Bonatti et al. [26, 33] proposed a biased functional based shape optimization for generating new families of elastically-isotropic open-cell shell-lattices. Soyarslan et al. [34] developed a parametric shape control method based on the periodic nodal surface to achieve elastically-isotropic shell-lattices. Chen et al. [27] and Deng et al. [35] proposed several elastically-isotropic hybrid lattices by combination of different types of TPMS shell-lattices or combination of plate-lattices and TPMS shell-lattices, while such combinations change the open-cell topology to closed-cell and additional holes have to be added to make the lattices manufacturable. Callens et al. [36] proposed a parametric metamaterial design strategy and achieved elastically-isotropic TPMS shell-lattices through multi-material hyperbolic tiling. The related work either changes the shape of the shell mid-surface away from minimal surface [26, 33, 34], or divides the lattice into several components with different lattice types or material properties [27, 35, 36]. Given the existing simulation results that shell-lattices with minimal surface geometry can approach the HS upper bound of bulk modulus [27], it turns out to be an inspiring goal to find open-cell, single-material and elastically-isotropic shell-lattices which maintain the minimal surface as the shell mid-surface to achieve superior stiffness.

In this work, a family of elastically-isotropic open-cell variable thickness TPMS shell-lattices are designed. The elastic anisotropy of a TPMS shell-lattice is tuned by smoothly varying its shell thickness with a strain energy-based numerical homogenization and optimization procedure. As a result, five types of elastically-isotropic TPMS shell-lattices are generated, among which N14 and OCTO are found to maintain over 90% of the HS upper bound of bulk modulus. All the optimized shell-lattices exhibit superior stiffness properties and significantly outperform elastically-isotropic truss-lattices. The elastically-isotropic N14 shell-lattices and the conventional counterparts of uniform thickness are fabricated with the micro laser powder bed fusion (LPBF) techniques in stainless steel 316L (SS316L). Quasi-static compression tests are conducted to investigate the Young's moduli, strength, and failure deformation behaviors along the three principal lattice directions ([100], [110] and [111]) and to validate the elastic isotropy of the variable thickness designs.

2. Elastically-isotropic design of TPMS shell-lattices

2.1 TPMS shell-lattices

In mathematics, a TPMS is a triply periodic surface with constant zero mean curvature. The Enneper-Weierstrass representation gives the accurate coordinates of the TPMS [37], while the Weierstrass function is only known for several types of TPMS. Alternatively, the TPMS is usually approximated by the periodic nodal surface with enough Fourier terms, which enables much easier generation of TPMS but the zero mean curvature may not be guaranteed [38]. Surface Evolver is a powerful tool for generating discrete TPMS [39], minimizing the surface tension energy of a surface with the prescribed boundary conditions and eventually leading to a TPMS with good accuracy. In this work, an accurate TPMS is generated in stereolithography (STL) format with the

use of Surface Evolver and then used as the shell mid-surface for finite element analysis (FEA) and optimization to achieve elastically-isotropic shell-lattices via variable thickness design.

This work focuses on the TPMS with cubic symmetry, i.e., with mirror symmetry about the three mid-planes and orthogonal rotational symmetry about the three axes. The former symmetry enables a unit cell to be decomposed into 8 equal parts, while the latter symmetry further divides each 1/8 cell into 6 smaller equal parts. As a result, the 1/48 domain (quadrilateral tetrahedron) is a fundamental unit of the unit cell, based on which the 1/8 cell and unit cell can be generated by mirror operations. Five types of TPMS are shown in Fig. 1, including N14, OCTO, IWP (I-graph-wrapped package), FRD (Face-centered cubic rhombic dodecahedron) and N (Neovius) surfaces, to illustrate the 1/48 fundamental unit (red), 1/8 cell (blue) and unit cell (grey), respectively. The 1/8 cell can be generated by mirroring the 1/48 fundamental unit about the neighboring edges, while the unit cell can be generated by mirroring the 1/8 cell about the three mid-planes.

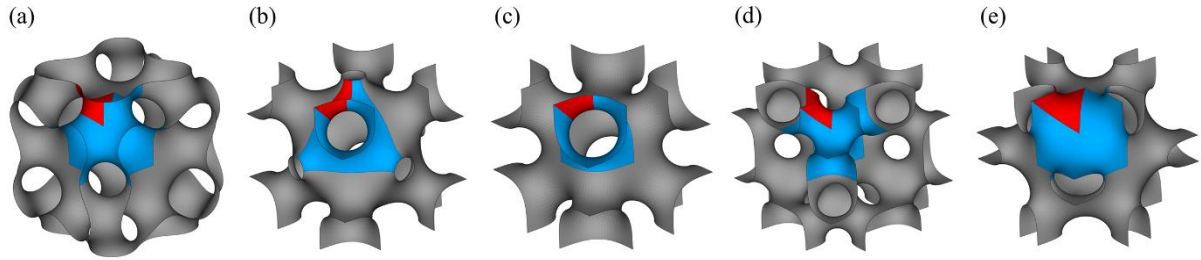


Fig. 1 Five types of TPMS, including: (a) N14, (b) OCTO, (c) IWP, (d) FRD and (e) N, with red, blue and grey colors representing the 1/48 fundamental unit, 1/8 cell and unit cell.

2.2 Elasticity of cubic symmetric lattices

The macroscopic constitutive relation of cubic symmetric lattices is represented as [40]:

$$\boldsymbol{\sigma} = \mathbf{C} \boldsymbol{\varepsilon} \quad (1)$$

where the macroscopic stress $\boldsymbol{\sigma}$, homogenized elasticity tensor \mathbf{C} and macroscopic strain $\boldsymbol{\varepsilon}$ are:

$$\boldsymbol{\sigma} = \begin{pmatrix} \sigma_{11} \\ \sigma_{22} \\ \sigma_{33} \\ \sigma_{23} \\ \sigma_{12} \\ \sigma_{13} \end{pmatrix}, \quad \mathbf{C} = \begin{pmatrix} c_{11} & c_{12} & c_{12} & 0 & 0 & 0 \\ c_{12} & c_{11} & c_{12} & 0 & 0 & 0 \\ c_{12} & c_{12} & c_{11} & 0 & 0 & 0 \\ 0 & 0 & 0 & c_{44} & 0 & 0 \\ 0 & 0 & 0 & 0 & c_{44} & 0 \\ 0 & 0 & 0 & 0 & 0 & c_{44} \end{pmatrix}, \quad \boldsymbol{\varepsilon} = \begin{pmatrix} \varepsilon_{11} \\ \varepsilon_{22} \\ \varepsilon_{33} \\ \gamma_{23} \\ \gamma_{12} \\ \gamma_{13} \end{pmatrix} \quad (2)$$

where c_{11} , c_{12} and c_{44} are three independent elasticity constants which completely define the stiffness properties of cubic symmetric lattices. The elastic anisotropy is typically assessed with the Zener anisotropic index ξ :

$$\xi = \frac{2c_{44}}{c_{11} - c_{12}} \quad (3)$$

where the Zener anisotropic index $\xi = 1$ corresponds to elastic isotropy.

Typically, three load cases are adopted for evaluation of the three elasticity constants, including the uniaxial strain loading, hydrostatic loading and shear loading. For all the three load cases, a unit strain is usually taken, meaning:

$$\boldsymbol{\varepsilon}^{(U)} = \begin{pmatrix} 1 \\ 0 \\ 0 \\ 0 \\ 0 \\ 0 \end{pmatrix}, \quad \boldsymbol{\varepsilon}^{(T)} = \begin{pmatrix} 1 \\ 1 \\ 1 \\ 0 \\ 0 \\ 0 \end{pmatrix}, \quad \boldsymbol{\varepsilon}^{(S)} = \begin{pmatrix} 0 \\ 0 \\ 0 \\ 0 \\ 1 \\ 0 \end{pmatrix}, \quad (4)$$

where the superscripts (U) , (T) and (S) correspond to the uniaxial strain loading, hydrostatic loading and shear loading, respectively. Based on Eq. (1) and (2), the three elasticity constants are obtained as:

$$\begin{aligned} c_{11} &= \sigma_{11}^{(U)}, \\ c_{12} &= \sigma_{22}^{(U)} = \sigma_{33}^{(U)}, \\ c_{44} &= \sigma_{12}^{(S)}, \\ c_{11} + 2c_{12} &= \sigma_{11}^{(T)} = \sigma_{22}^{(T)} = \sigma_{33}^{(T)}, \end{aligned} \quad (5)$$

where $\sigma_{11}^{(U)}$, $\sigma_{22}^{(U)}$, $\sigma_{33}^{(U)}$, $\sigma_{12}^{(S)}$, $\sigma_{11}^{(T)}$, $\sigma_{22}^{(T)}$ and $\sigma_{33}^{(T)}$ are the macroscopic stress components of the corresponding load cases. Although only two load cases (uniaxial strain loading and shear loading) are enough for determining all the three elasticity constants, the hydrostatic loading is necessary for the sensitivity analysis of the optimization problem to achieve elastic isotropy, as detailed in the sub-section 2.4. In addition, the hydrostatic loading serves as a verification of the two elasticity constants c_{11} and c_{12} obtained from the uniaxial strain loading. To evaluate the macroscopic stresses σ_{11} , σ_{22} , σ_{33} and σ_{12} in Eq. (5), two expressions are adopted based on Hill's principle [40]:

$$\boldsymbol{\sigma} = \frac{1}{A} \int_A d\mathbf{F}, \quad (6a)$$

$$\boldsymbol{\sigma} = \frac{1}{V} \int_V \boldsymbol{\sigma}_\mu dV, \quad (6b)$$

where A , V are the end face area and volume of the selected representative volume element, \mathbf{F} is the reaction force on the end faces, while $\boldsymbol{\sigma}_\mu$ is the microscopic stress. Eq. (6a) represents the

average stress over the end faces and is called the macroscopic average stress, while Eq. (6b) represents the average stress over the entire volume of the representative element and is called the microscopic average stress. The Hill's principle reveals that the macroscopic average stress is equal to the microscopic average stress [40].

As shown in the sub-section 2.4, a strain energy-based optimization algorithm is proposed in this work for achieving elastically-isotropic shell-lattices, while the elasticity constants in Eq. (5) are in terms of the macroscopic stresses. For derivation of the sensitivity, the elasticity constants are rewritten in terms of the strain energy. To achieve this, the strain energies of the three load cases are first obtained in terms of the macroscopic stresses as:

$$e^{(U)} = \frac{1}{2} \sigma_{11}^{(U)} V, \quad (7a)$$

$$e^{(T)} = \frac{1}{2} [\sigma_{11}^{(T)} + \sigma_{22}^{(T)} + \sigma_{33}^{(T)}] V, \quad (7b)$$

$$e^{(S)} = \frac{1}{2} \sigma_{12}^{(S)} V, \quad (7c)$$

Based on Eq. (5), the strain energies in Eq. (7a) ~ (7c) are rewritten in terms of the elasticity constants as:

$$e^{(U)} = \frac{1}{2} c_{11} V, \quad (8a)$$

$$e^{(T)} = \frac{3}{2} (c_{11} + 2c_{12}) V, \quad (8b)$$

$$e^{(S)} = \frac{1}{2} c_{44} V, \quad (8c)$$

Thus, the elasticity constants in Eq. (5) are rewritten in terms of the strain energy as:

$$c_{11} = \frac{2}{V} e^{(U)}, \quad (9a)$$

$$c_{12} = \frac{1}{V} \left[\frac{1}{3} e^{(T)} - e^{(U)} \right], \quad (9b)$$

$$c_{44} = \frac{2}{V} e^{(S)}, \quad (9c)$$

2.3 FEA implementation

To evaluate the three elasticity constants, FEA under the three load cases above are performed. A representative unit cell is typically selected for FEA, with the periodic boundary conditions imposed [40-42]. Due to the cubic symmetry of the TPMS considered in this work, the 1/8 cell is selected for linear elastic analysis to save the computational cost without loss of accuracy. For uniaxial strain loading and hydrostatic loading, the symmetry boundary conditions are imposed on the three mid-planes. For shear loading, the anti-symmetry boundary conditions are imposed on

the two mid-planes bearing the shear loading, while the symmetry boundary condition is imposed on the third mid-plane. Thus, the boundary conditions imposed on the other three end planes for all the three load cases can be derived by simplifying the expressions of the periodic boundary conditions.

This work adopts the ABAQUS STRI3 shell element for linear elastic analysis, based on the classical Kirchhoff-Love plate/shell theory. The constituent material is assumed to be isotropic in stiffness, with the Young's modulus $E_s = 190$ GPa and Poisson's ratio $\nu_s = 0.3$. For ease of FEA implementation, Eq. (6a) is adopted for evaluation of the macroscopic stress σ , implemented as:

$$\sigma = \frac{1}{A} \sum_{i=1}^n \mathbf{F}_i^R, \quad (10)$$

where \mathbf{F}_i^R is the reaction force in the direction of the applied displacement, while n is the number of nodes on the corresponding end faces. To achieve the macroscopic stiffness properties, the macroscopic stress is first evaluated by Eq. (10), based on which the strain energies of the three load cases are obtained by Eq. (7a) ~ (7c). The three elasticity constants and Zener anisotropic index are then evaluated by Eq. (9a) ~ (9c) and Eq. (3).

2.4 Elastically-isotropic TPMS shell-lattices via variable thickness design

In this work, a family of elastically-isotropic TPMS shell-lattices are proposed via variable thickness design, based on the following optimization problem:

$$\begin{cases} \min_{\delta_i} J = \frac{1}{2}(\xi - 1)^2, \quad (i = 1, 2, \dots, N) \\ \text{s.t.} \begin{cases} a(\mathbf{u}^{(j)}, \mathbf{v}^{(j)}) = l(\mathbf{v}^{(j)}), \quad \forall \mathbf{v}^{(j)} \in \mathbf{U}, \quad (j = U, T, S) \\ \delta_{\min} \leq \delta_i \leq \delta_{\max}, \quad (i = 1, 2, \dots, N) \end{cases} \end{cases} \quad (11)$$

where the shell mid-surface is discretized into N triangular elements, each of which is assigned with the thickness of δ_i . The objective function J is defined in terms of the Zener anisotropic index ξ . The static equilibrium is given in the weak variational form in terms of the energy bilinear form $a(\mathbf{u}^{(j)}, \mathbf{v}^{(j)})$ and load linear form $l(\mathbf{v}^{(j)})$, where $\mathbf{u}^{(j)}$ and $\mathbf{v}^{(j)}$ denote the displacement field and virtual displacement field of load case j , while \mathbf{U} denotes the kinematically admissible displacement field. δ_{\min} and δ_{\max} denote the minimum and maximum thickness of the shell-lattice and are selected properly to satisfy the manufacturing constraints and thin shell assumption.

The sensitivity derivation and updating scheme of the shell thickness are detailed in the *Appendix*. The initial design is adopted as the uniform thickness TPMS shell-lattices. In the optimization process, the 1/8 cell is taken as the FEA domain, while the 1/48 fundamental unit is taken as the design domain. As discussed previously, the 1/8 cell consists of 6 fundamental domains, each of which can be generated as the mirror image of the neighboring fundamental

domain. Since the strain energy distributions as well as the sensitivities of the 6 fundamental domains are not identical, an average operation of the sensitivity terms is performed in each iteration step to maintain cubic symmetry, i.e.,

$$\overline{\frac{\partial J}{\partial \delta_i}} = \frac{1}{6} \sum_{k=1}^6 \frac{\partial J}{\partial \delta_i}^{(k)}, \quad (i = 1, 2, \dots, N) \quad (12)$$

where the superscript (k) denotes the k -th fundamental domain within the 1/8 cell. The averaged sensitivity terms $\overline{\frac{\partial J}{\partial \delta_i}}$ are then adopted for updating the shell thickness by Eq. (A8) and (A9). The tolerance for convergence of the Zener anisotropic index is set as 0.01.

2.5 Variable-thickness offset operation

After the optimization iteration converges, a variable-thickness offset operation is performed by MATLAB programming to export the final design in STL format. First, the thickness of each node is taken as the average of the thicknesses of neighboring triangular elements. Then, the top and bottom surfaces are generated by offsetting every mid-surface node along its positive and negative normal directions for a half of the nodal thickness. A variable thickness shell-lattice is then obtained by combining the top and bottom surfaces with the lateral surfaces.

3. Experimental methods

3.1 Micro-LPBF

To validate the stiffness properties, the uniform and variable thickness N14 shell-lattices were fabricated on the *Hans' Laser M100* machine equipped with 500W IPG fiber laser ($\lambda = 1.07 \mu\text{m}$) with the beam diameter of $25 \mu\text{m}$. All the lattices were fabricated using the gas atomized austenitic SS316L powder provided by Beijing AMC Powder Metallurgy Technology Co., Ltd. The particle size of the powder is within the range of $5\text{-}25 \mu\text{m}$ ($D_{50} = 16.27 \mu\text{m}$) and its chemical compositions are listed in Table 1. The laser power, scanning speed, hatch distance and layer thickness are 50 W, 1000 mm/s, $50 \mu\text{m}$ and $10 \mu\text{m}$, respectively. A common scanning strategy was adopted to reduce the thermal stress by rotating the patterns between successive layers for a hatch angle of 67° . The micro-LPBF fabricated SS316L has the density of $\rho_s = 8.03 \text{ g/cm}^3$ and Young's modulus of $E_s = 190 \text{ GPa}$, based on the in-house standard tensile tests of tensile specimens, in which the loading direction is within the platform (x - y) plane.

Table 1 Chemical compositions of SS316L

Element	Cr	Ni	Mo	Mn	Si	P	S	C	O	Fe
wt. %	16.88	13.6	2.7	0.54	0.41	0.012	0.0063	0.0066	0.0875	Bal.

3.2 Test specimens and fabrication orientations

The details of the lattice designs including the thicknesses, dimensions and relative densities are listed in Table 2, in which 3 groups of the lattice directions of [100], [110] and [111] were fabricated. In each group, 6 specimens were built, including 3 variable thickness lattices and 3 uniform thickness ones with the same designed relative density ($\bar{\rho} = 10.55\%$) for comparison. Thus, a total number of 18 specimens were prepared for experimental tests, whose relative densities were measured by the dry weight method and also included in Table 2. The low relative standard deviations of the measured relative densities for all groups reveal good fabrication accuracy. The fabrication orientations and specimens built by micro-LPBF along [100], [110] and [111] directions are shown in Fig. 2, in which the lattice directions are labelled by arrows. The material and lattice directions are further illustrated in Table 3, in which the material direction represents the direction in the platform coordinate system shown in Fig. 2. According to the rules of Miller indices, a negative number in the lattice direction is represented by a bar over it. It is noted that the material directions of [100] and [110] specimens were aligned with the lattice directions, while those of [111] specimens were no longer aligned with the lattice directions since the specimens were rotated to save the fabrication space.

To verify the thickness distribution of the as-printed lattices, the uniform and variable thickness [100] specimens were examined by the scanning electron microscope (SEM) using the *JSM-7800F* field emission SEM system. The SEM images of the top surfaces are shown in Fig. 3, which demonstrates the uniform thickness distribution in Fig. 3 (a) and variable thickness distribution in Fig. 3 (b).

Table 2 Design and measured parameters of uniform and variable thickness N14 shell-lattices

	Uniform thickness			Variable thickness		
Designed thickness δ (μm)	122			100 ~ 250		
Designed relative density $\bar{\rho}$	10.55%			10.55%		
Lattice direction	[100]	[110]	[111]	[100]	[110]	[111]
Measured relative density $\bar{\rho}$	12.84 ± 0.31 %	13.03 ± 0.40 %	13.74 ± 0.63 %	13.88 ± 0.43 %	14.11 ± 0.50 %	12.88 ± 0.34 %
Unit cell size $D_1 \times D_2 \times D_3$ (mm)	$5 \times 5 \times 5$	$7.07 \times 7.07 \times 5$	$8.66 \times 7.07 \times 12.25$	$5 \times 5 \times 5$	$7.07 \times 7.07 \times 5$	$8.66 \times 7.07 \times 12.25$
No. of unit cells	$5 \times 5 \times 5$	$4 \times 4 \times 5$	$3 \times 4 \times 2.5$	$5 \times 5 \times 5$	$4 \times 4 \times 5$	$3 \times 4 \times 2.5$
Total size $L_1 \times L_2 \times L_3$ (mm)	$25 \times 25 \times 25$	$28.28 \times 28.28 \times 30.62$	$25.98 \times 28.28 \times 30.62$	$25 \times 25 \times 25$	$28.28 \times 28.28 \times 25$	$25.98 \times 28.28 \times 30.62$

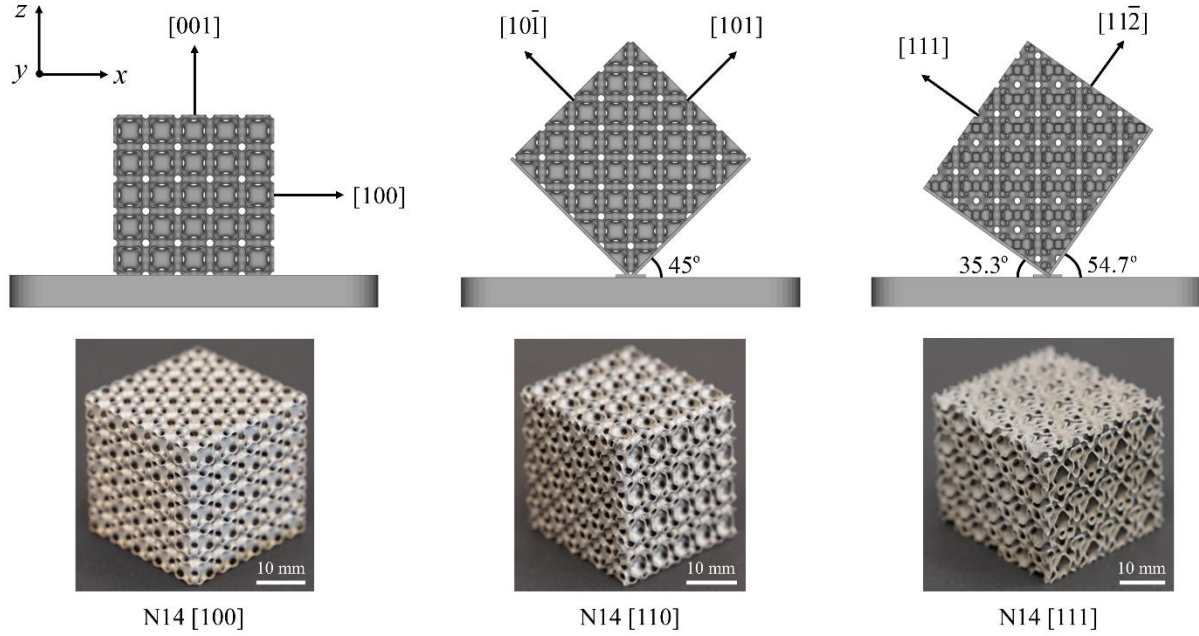


Fig. 2 Fabrication orientations and specimens built by micro-LPBF along [100], [110] and [111] directions. (The lattice directions are labelled by arrows in the figure.)

Table 3 Material and lattice directions of [100], [110] and [111] specimens

[100] specimen		[110] specimen		[111] specimen	
Material direction	Lattice direction	Material direction	Lattice direction	Material direction	Lattice direction
(1, 0, 0)	[100]	(1, 0, 1)	[101]	(0, 1, 0)	[1̄10]
(0, 1, 0)	[010]	(1, 0, -1)	[10̄1]	(-0.816, 0, 0.577)	[111]
(0, 0, 1)	[001]	(0, 1, 0)	[010]	(0.577, 0, 0.816)	[112̄]

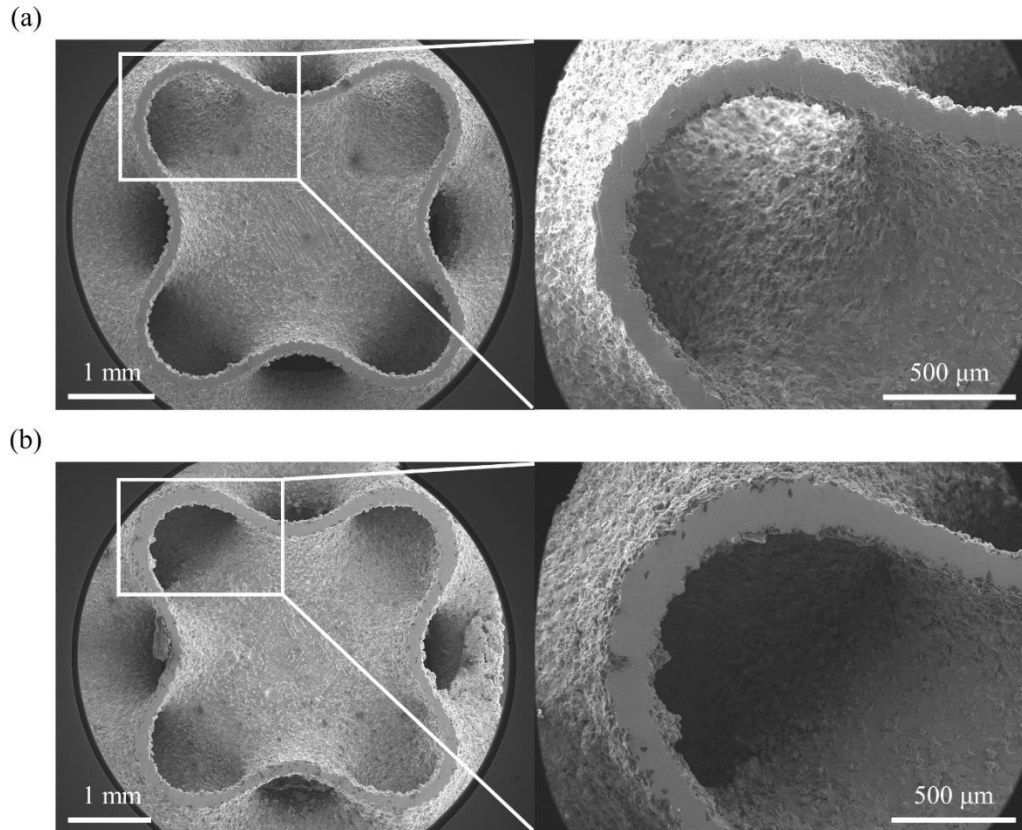


Fig. 3 SEM images of [100] specimens: (a) uniform thickness lattice, (b) variable thickness lattice.

3.3 Compression tests of elasticity

To test the Young's moduli of the lattices, the *Instron E10000* universal testing system with a 10 kN load cell was used. For brevity of expression, the uniform/variable thickness [100] specimens are denoted as U100/V100, and so forth. In each compression test, the specimen was loaded up to 6 kN with a speed of 0.75 mm/min (corresponding to a strain rate of $4.07 \times 10^{-4} \sim 5.07 \times 10^{-4} / \text{s}$) and unloaded with the same speed. All specimens were within the linear elastic region during the load-unload tests. For each specimen, the compression tests were

conducted along all the 3 orthogonal directions. Typically, the compression response of the first loading test deviates from the subsequent ones to some extent due to non-flat surfaces and local yielding, while those of the second and later tests show a good repeatability and the slopes are consistent with the unload slope of the first test, as shown in Fig. 4 for the test of U100 specimen along [100] direction. Thus, the compression test along each direction was conducted for 4 times, with the specimens rotated along the loading axis for 90° each time. The compressive strain of the lattices was calculated by $\varepsilon = d / h$, where d denotes the crosshead displacement, while h denotes the height of the specimen. The compressive load was measured by the load cell, and the compressive stress was calculated by $\sigma = P / A_0$, where P denotes the compressive load, while A_0 denotes the end face area of the specimen. Since the unload curves were more stable than load curves, the Young's modulus of the lattices along each direction was calculated as the average of the 4 unload slopes of the stress-strain curves, denoted as k_{m+s} . It should be noted that the deformations of machine and fixtures were included in the crosshead experiments, so the moduli of the lattices were underestimated. To eliminate this underestimation, the machine stiffness was measured by compression tests of the machine itself, following the same load-unload procedure. The compression tests were conducted for 3 times, and the machine stiffness was evaluated as the average of the 3 unload slopes of the load-displacement curves, denoted as k_m . Thus, the Young's modulus of the lattices was corrected by:

$$E = \frac{hk_m k_{m+s}}{hk_m - A_0 k_{m+s}} \quad (13)$$

Eq. (13) was then adopted for evaluation of the Young's moduli of the specimens.

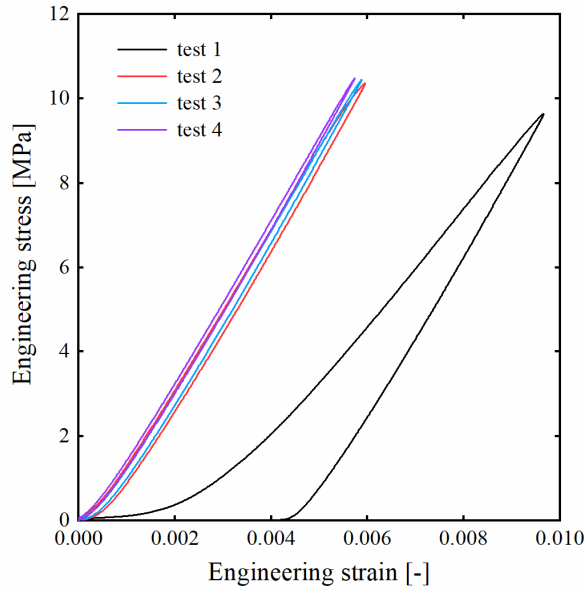


Fig. 4 Stress-strain curves of small strain compression test along [100] direction for U100 specimen.

3.4 Large strain compression tests

To test the failure behavior and energy absorption performance of the lattices, the *MTS ALLIANCE RT/50* testing machine with a 50 kN load cell was used. The tests were conducted along the lattice direction [100] for U100/V100 specimens, [110] for U110/V110 specimens, and [111] for U111/V111 specimens, respectively. In each test, the specimen was loaded up to 45 kN with a compressive speed of 1.5 mm/min (corresponding to a strain rate of $8.89 \times 10^{-4} \sim 1.01 \times 10^{-3} / \text{s}$). The compressive strain and stress were measured from the crosshead displacement and load cell, respectively. The deformations of the lattices were recorded by an *EOS 6D* full frame digital single-lens reflex camera with a frequency of 0.1 Hz. The normalized plateau stress (NPS) σ_p was explored as an indicator of the plasticity, which was defined as the average stress within the strain range of [0.2, 0.4] normalized by the relative density [43]:

$$\sigma_p = \frac{5}{\rho} \int_{0.2}^{0.4} \sigma(e) de \quad (14)$$

Besides, the energy absorption performance of the lattices was also studied. Based on the stress-strain curve of the uniaxial compression test, the energy absorption efficiency was calculated as [44]:

$$\eta(\varepsilon) = \frac{1}{\sigma(\varepsilon)} \int_0^{\varepsilon} \sigma(e) de \quad (15)$$

The strain with the maximum efficiency was then extracted, denoted as ε_d , based on which the specific energy absorption (SEA) was evaluated as:

$$\psi = \frac{1}{\rho} \int_0^{\varepsilon_d} \sigma(e) de \quad (16)$$

to measure the energy absorption capacity of the lattices.

4. Results and discussions

4.1 Elastically-isotropic designs

The five types of TPMS in Fig. 1 are adopted for seeking elastically-isotropic shell-lattices based on the optimization problem (11). The unit cell size is taken as $D = 2 \text{ mm}$, while the initial design is taken as the uniform thickness lattice with the thickness of $\delta = 0.04 \text{ mm}$, corresponding to an aspect ratio δ / D (i.e., shell thickness to unit cell size ratio) of 1/50.

The optimized elastically-isotropic shell-lattices are plotted in Fig. 5, with the thickness distribution and views of the 1/48 fundamental unit, 1/8 cell and unit cell. The lower bound δ_{\min} is taken as $(1/50)D$ for N14 and OCTO lattices, $(1/100)D$ for IWP and FRD lattices, and $(1/200)D$ for N lattice, while the upper bound δ_{\max} is taken as $(1/20)D$ for all the five types of

TPMS lattices to obtain elastically-isotropic designs ($|\xi - 1| < 0.01$). The geometry and mechanical data of the uniform and variable thickness lattices are listed in Table 4, in which ν , E , G and K denote the Poisson's ratio, Young's, shear and bulk moduli. The normalized Young's modulus $E/(\bar{\rho}E_s)$, shear modulus $G/(\bar{\rho}E_s)$ and bulk modulus $K/(\bar{\rho}E_s)$ are compared with the HS upper bounds in low relative densities (0.499, 0.202 and 0.317). All the uniform thickness TPMS shell-lattices can reach the HS upper bound of bulk modulus in low relative densities [27]. It is noted that the low elastic anisotropy of the uniform thickness N14/OCTO shell-lattices ($\xi = 0.827/0.617$) makes it easier to achieve elastic isotropy by varying the shell thickness, with the Young's, shear and bulk moduli reaching 61.32%/62.73%, 56.58%/58.07% and 97.82%/93.50% of the HS upper bounds, respectively. That is to say, the elastically-isotropic N14/OCTO shell-lattices maintain over 90% of the HS upper bound of bulk modulus. On the other hand, the higher elastic anisotropy of the uniform thickness IWP/FRD/N shell-lattices ($\xi = 0.592/0.531/0.390$) makes it harder to achieve elastic isotropy by varying the shell thickness. Smaller lower bounds δ_{\min} are therefore adopted for the optimization algorithm to obtain elastically-isotropic designs, with the Young's, shear and bulk moduli reaching 54.05%/50.68%/45.69%, 50.74%/46.90%/42.04% and 73.97%/74.95%/70.35% of the HS upper bounds, respectively. Thus, the bulk moduli of the elastically-isotropic IWP/FRD/N shell-lattices are lower than those of N14/OCTO, as a result of the larger deviation from uniform thickness. In general, the elastically-isotropic variable thickness TPMS shell-lattices possess lower Young's and bulk moduli and higher shear moduli than uniform thickness ones.

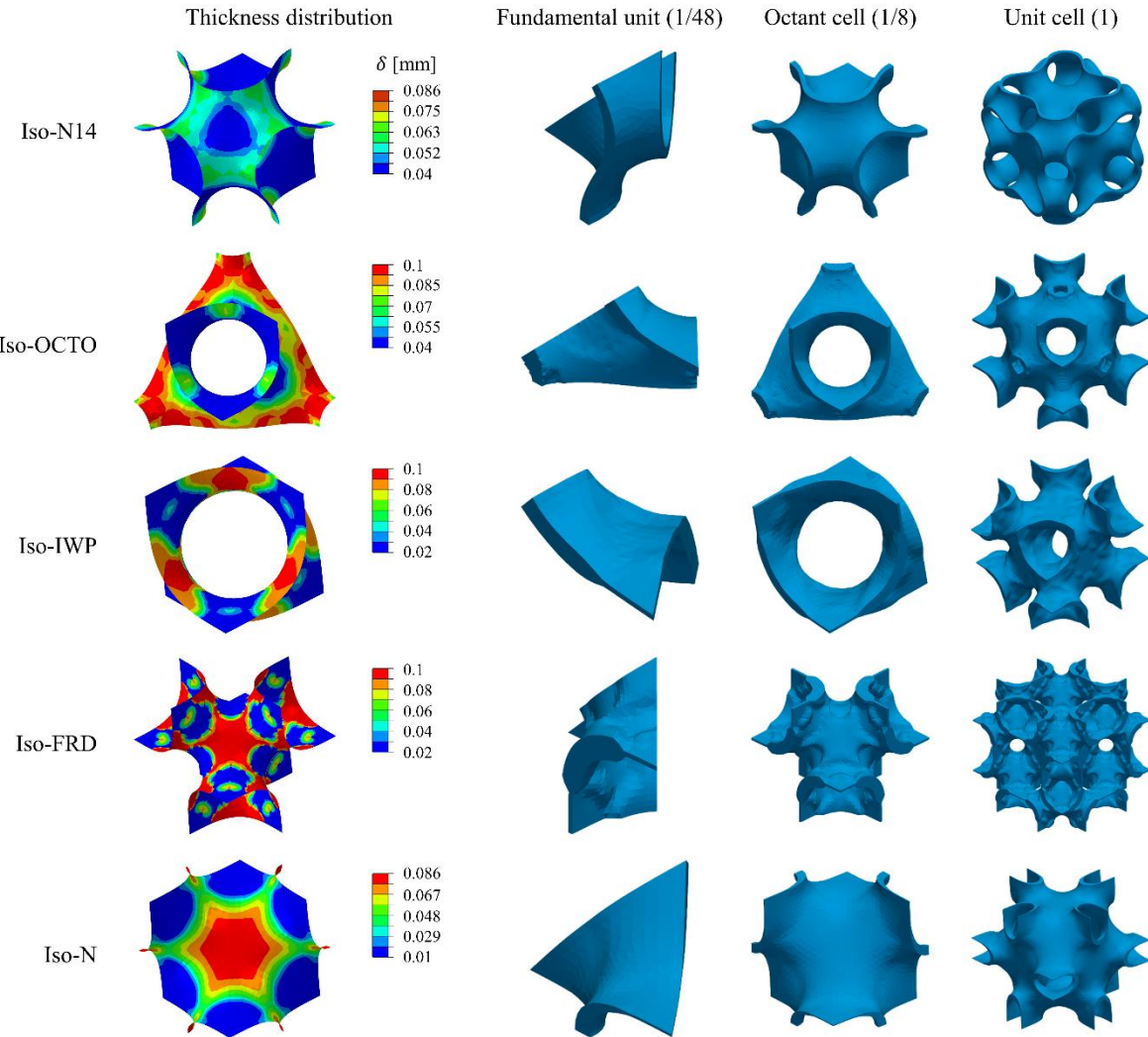


Fig. 5 Elastically-isotropic shell-lattices: thickness distribution and views of the 1/48 fundamental unit, 1/8 cell and unit cell. (Iso-N14 represents elastically-isotropic N14 shell-lattices, and so forth.)

Table 4 Geometry and mechanical data of uniform and variable thickness TPMS shell-lattices

Property	Uniform thickness					Variable thickness				
	N14	OCTO	IWP	FRD	N	N14	OCTO	IWP	FRD	N
$\bar{\rho}$	8.68%	7.33%	6.93%	9.55%	7.03%	10.55%	11.50%	8.85%	14.20%	6.45%
ξ	0.827	0.617	0.592	0.531	0.390	0.994	0.992	0.995	0.991	0.990
ν	0.323	0.308	0.278	0.280	0.298	0.335	0.324	0.308	0.323	0.330
$E / (\bar{\rho}E_s)$	0.337	0.367	0.423	0.419	0.384	0.306	0.313	0.270	0.253	0.228
$G / (\bar{\rho}E_s)$	0.105	0.087	0.098	0.087	0.058	0.114	0.117	0.103	0.095	0.085
$K / (\bar{\rho}E_s)$	0.318	0.318	0.318	0.317	0.317	0.310	0.296	0.235	0.238	0.223

4.2 Stiffness comparison of low-density lattices

The stiffness properties of the five types of elastically-isotropic shell-lattices are compared with the elastically-isotropic truss-lattices and plate-lattices, as summarized in Fig. 6. The Young's, shear and bulk moduli of the optimal elastically-isotropic plate-lattices are found to reach the HS upper bounds in low relative densities [15-17], while those of the optimal elastically-isotropic truss-lattices can only reach nearly 1/3 of the HS upper bounds [12-14], as shown in the shaded grey region in Fig. 6. By comparison, the bulk moduli of the elastically-isotropic N14/OCTO shell-lattices nearly attain the HS upper bounds, while those of the elastically-isotropic IWP/FRD/N shell-lattices reach nearly 70% of the HS upper bounds. The Young's moduli of the five types of elastically-isotropic TPMS shell-lattices reach nearly 50% ~ 60% of the HS upper bounds, while their shear moduli reach nearly 40% ~ 60% of the HS upper bounds. The elastically-isotropic shell-lattices exhibit superior stiffness properties and significantly outperform elastically-isotropic truss-lattices, while their stiffness properties are lower than the elastically-isotropic plate-lattices, as a trade-off induced by the open-cell topology. In general, the elastically-isotropic plate-lattices maximize the stiffness properties of porous cellular solids in low relative densities, while their closed-cell topology complicates the manufacturing and applications in specified industries. The elastically-isotropic shell-lattices developed in this work exhibit superior stiffness properties and maintain the open-cell topology. The opportunities for shell-lattices are given in the unshaded grey region in Fig. 6, while the detailed upper limits of their stiffness properties remain to be explored. Thus, it is an ongoing research topic to develop elastically-isotropic open-cell shell-lattices with stiffness properties closer to the HS upper bounds.

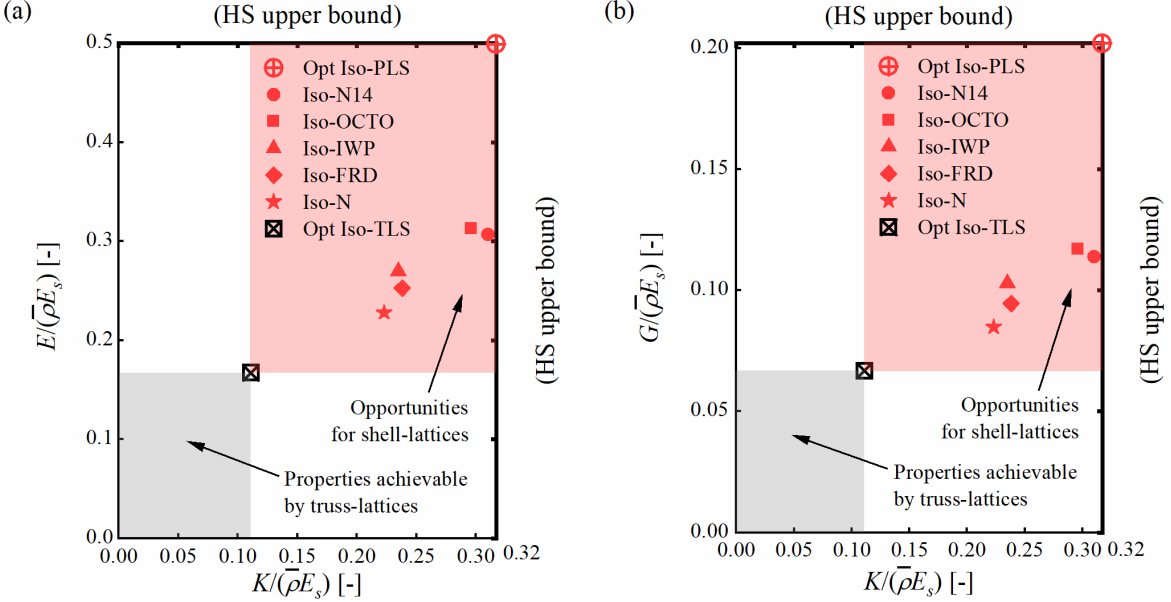


Fig. 6 Comparisons of the stiffness properties of elastically-isotropic plate-lattices, shell-lattices and truss-lattices: (a) normalized Young's modulus versus normalized bulk modulus, (b) normalized shear modulus versus normalized bulk modulus, in which *Opt Iso-PLS*, *Opt Iso-TLS* represent optimal elastically-isotropic plate-lattices and truss-lattices, respectively.

4.3 Experimental results of elasticity

The experimental and FEA results of the normalized Young's moduli of the uniform and variable thickness specimens are listed in Table 5. It is found that the multiple load-unload tests lead to high experimental repeatability. Theoretically, the Young's moduli along [100], [010] and [001] directions are the same, while comparisons of the experimental data along (1), (2) and (3) directions reveal that the Young's moduli along [100] and [010] directions are almost the same, which, however, are nearly 13% higher than that along [001] direction. Observations of the Young's moduli along (4), (5) and (7) directions reveal a similar trend. Thus, the anisotropy of the constituent material is observed and yields a detectable deviation of the stiffness properties. Since [001] is the building direction, while [100] and [010] lie in the platform (x - y) plane, two key observations are made that: (1) the LPBF fabricated material exhibits similar properties within the platform (x - y) plane, which are different from the building direction (z direction); (2) the larger the angle between the specified direction and platform plane, the lower the Young's modulus induced by the constituent material's anisotropy.

The normalized Young's moduli along all the 9 test directions for the uniform and variable thickness specimens are further illustrated in Fig. 7. The 9 tests are categorized into 5 groups, denoted as GR1-GR5, each of which has the same material direction and therefore the same material property along the test direction. For the test directions (1), (2), (6) and (7) within GR1, the material directions all lie in the platform plane. Since (1), (2) and (6) also possess the same lattice direction of [100], the tested normalized Young's moduli are almost the same, with an

average of 0.275/0.261 for the uniform/variable thickness specimens. However, (7) has a different lattice direction of [110], thus with the different normalized Young's moduli of 0.254/0.255. Therefore, the experimental data reveals a [100] to [110] moduli ratio of 1.08/1.02 for the uniform/variable thickness specimens, respectively. By comparison, the FEA gives the [100] to [110] moduli ratio as 1.12/1.00, which shows a reasonable agreement with the experimental results. In addition, the FEA gives the normalized [100] Young's moduli of 0.343/0.306 for the uniform/variable thickness specimens, showing 24.73%/17.24% relative differences with the experimental results; and normalized [110] Young's moduli of 0.306 for both specimens, showing 20.47%/20.00% relative differences. As a whole, the differences between experimental and FEA results are within an acceptable range, while the remaining discrepancy is attributed to: (1) the boundary conditions of multi-cell specimens in experiments are approximations to the periodic boundary conditions in FEA; (2) manufacturing imperfections such as surface roughness; (3) the anisotropy of the constituent material.

Besides, the experimental [100] to [110] moduli ratio reveals a reduced elastic anisotropy of the variable thickness specimens, with the ratio reduced from 1.08 of the uniform thickness specimens to 1.02 of the variable thickness ones. For the test direction (8) with the lattice direction of [111], and (9) with that of [11 $\bar{2}$], the material directions don't lie in the platform plane and has the intersection angles of 35.3° and 54.7°, respectively. Thus, the tested Young's moduli deviate more from FEA results, as a result of the anisotropy of the AM fabricated material. Overall, the maximum to minimum Young's moduli ratio of all the 9 test directions is reduced from 1.26 of the uniform thickness specimens to 1.20 of the variable thickness specimens. Although the overall anisotropy in stiffness is still observed in the variable thickness specimens due to the constituent material's anisotropy, it is validated that the elastic anisotropy is reduced by varying the shell thickness accordingly.

Table 5 Normalized Young's modulus of uniform and variable thickness N14 shell-lattices

Specimen	Test direction	Material direction	Lattice direction	$E / (\bar{\rho}E_s)$	
				Experimental	FEA
U100	(1)	(1, 0, 0)	[100]	0.279 ± 0.009	
	(2)	(0, 1, 0)	[010]	0.276 ± 0.001	0.343
	(3)	(0, 0, 1)	[001]	0.245 ± 0.005	
U110	(4)	(1, 0, 1)	[101]	0.224 ± 0.006	0.306
	(5)	(1, 0, -1)	[10̄1]	0.222 ± 0.006	0.306
	(6)	(0, 1, 0)	[010]	0.269 ± 0.025	0.343
U111	(7)	(0, 1, 0)	[11̄0]	0.254 ± 0.017	0.306
	(8)	(-0.816, 0, 0.577)	[111]	0.251 ± 0.013	0.295
	(9)	(0.577, 0, 0.816)	[11̄2]	0.227 ± 0.016	0.306
V100	(1)	(1, 0, 0)	[100]	0.259 ± 0.002	
	(2)	(0, 1, 0)	[010]	0.257 ± 0.011	0.306
	(3)	(0, 0, 1)	[001]	0.228 ± 0.006	
V110	(4)	(1, 0, 1)	[101]	0.222 ± 0.009	
	(5)	(1, 0, -1)	[10̄1]	0.221 ± 0.003	0.306
	(6)	(0, 1, 0)	[010]	0.266 ± 0.003	
V111	(7)	(0, 1, 0)	[11̄0]	0.255 ± 0.011	
	(8)	(-0.816, 0, 0.577)	[111]	0.238 ± 0.028	0.306
	(9)	(0.577, 0, 0.816)	[11̄2]	0.222 ± 0.009	

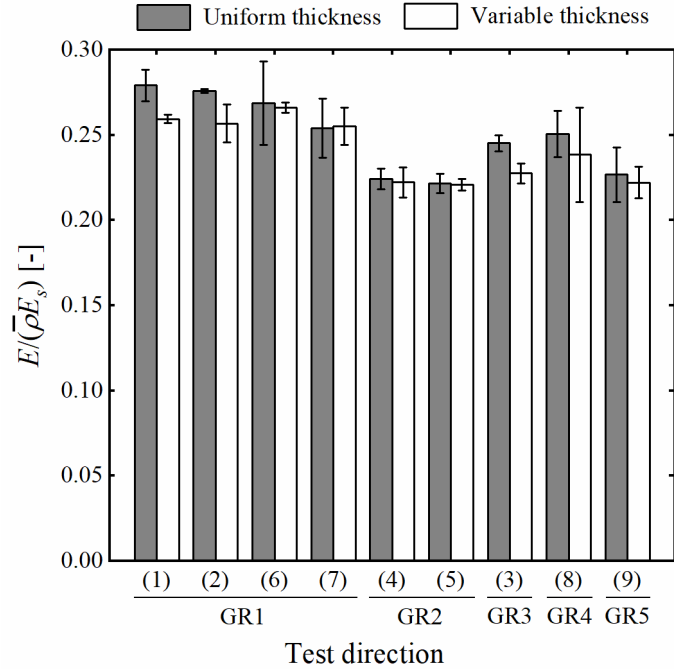


Fig. 7 Normalized Young's moduli along all the 9 test directions for the uniform and variable thickness specimens.

4.4 Experimental results of large strain compression

The stress-strain curves of large strain compression tests along the 3 lattice directions are plotted in Fig. 8, with the deformation patterns of the uniform thickness specimens shown in Fig. 9. Experimental results reveal that both uniform and variable thickness N14 lattices show different failure deformation behaviors along different directions. The thickness variations in this work have no significant influences on the failure deformations. It is noted that a layer-by-layer plastic buckling failure mode is observed in the compression tests along [100] direction in Fig. 9 (a), corresponding to 5 sudden drops in the stress-strain curves in Fig. 8 (a). However, no buckling deformation occurs in the compression tests along [110] and [111] directions, while the failures are related to the shear deformation. Thus, no sudden drops appear in the stress-strain curves in Fig. 8 (b) and Fig. 8 (c).

The NPS σ_p and SEA ψ are illustrated in Fig. 10, showing that the uniform thickness specimens possess the highest and lowest plateau stresses along [111] and [100] directions, respectively. The variable thickness ones possess the highest and lowest plateau stresses along [110] and [100] directions, respectively. The maximum to minimum plateau stress ratio is reduced from 1.21 of the uniform thickness specimens to 1.12 of the variable thickness ones, which reveals a reduced anisotropy of strength for the variable thickness specimens. Besides, observations of the SEA along the 3 directions reveal that the uniform thickness specimens possess the highest and lowest energy absorption capacities along [111] and [110] directions, respectively. The maximum to minimum SEA ratio is reduced from 1.23 of the uniform thickness specimens to 1.03 of the

variable thickness ones, which indicates that the variable thickness specimens can even achieve nearly isotropic energy absorption capacity.

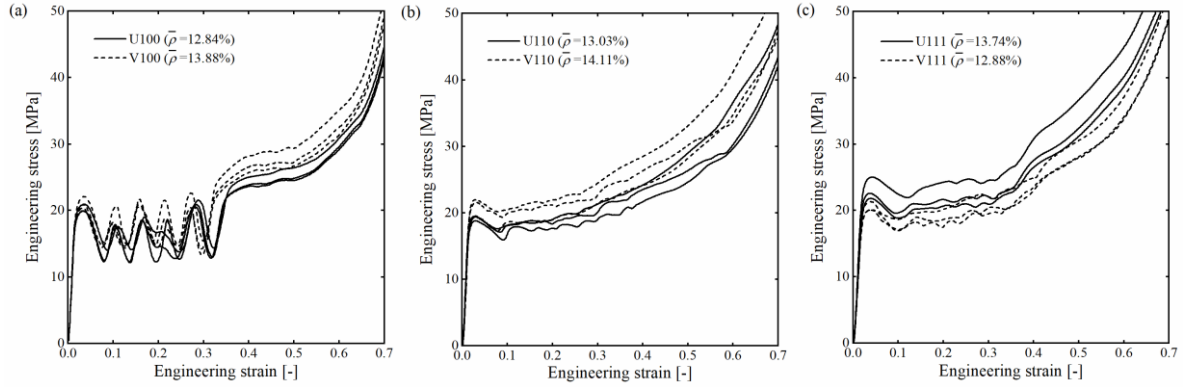


Fig. 8 Stress-strain curves of large strain compression tests along: (a) [100], (b) [110], (c) [111] directions.

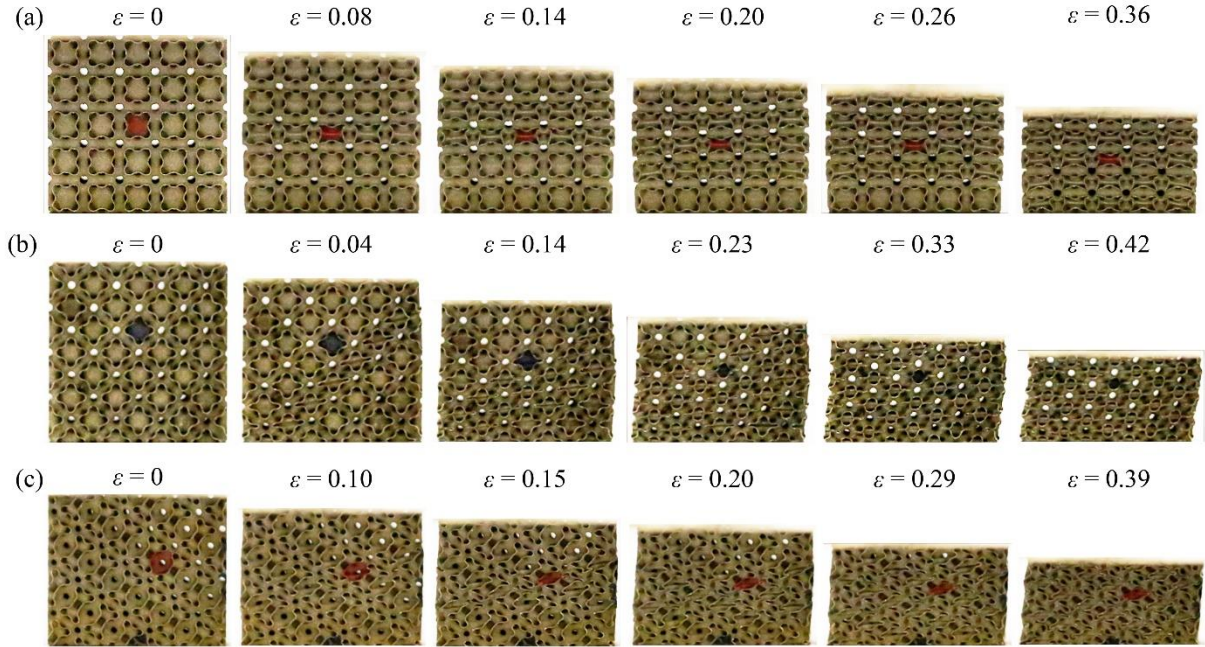


Fig. 9 Experimental large strain compressive deformation patterns for: (a) U100 specimen with a layer-by-layer plastic buckling failure mode, (b) U110 specimen with shear deformation failure, (c) U111 specimen with shear deformation failure. (The corresponding engineering strains are labelled in the figure.)

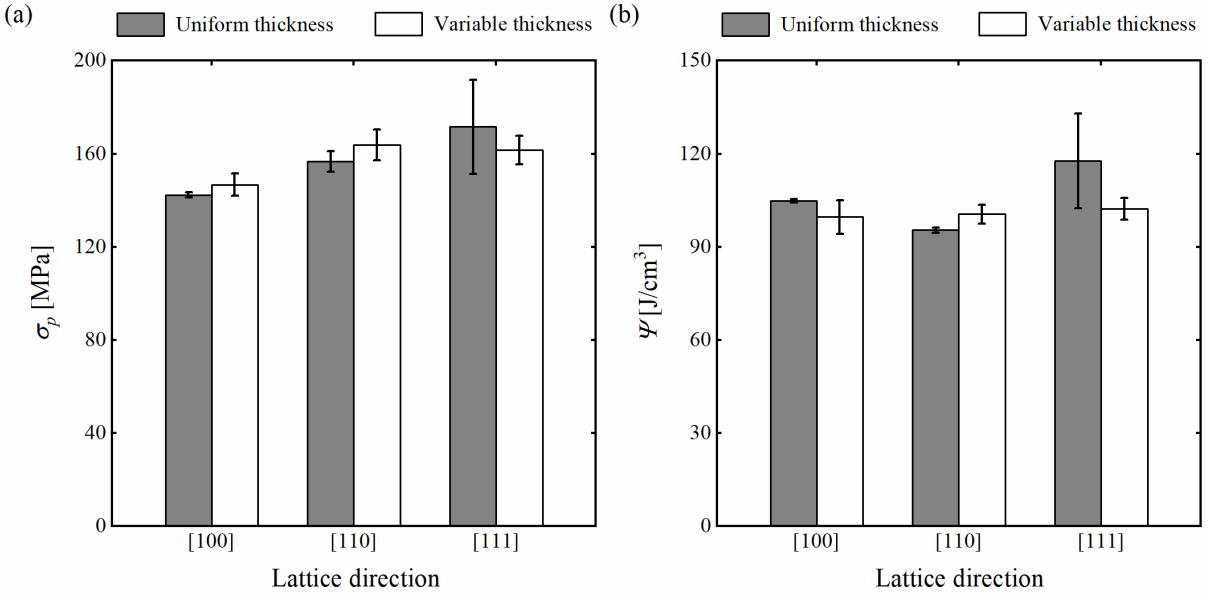


Fig. 10 (a) NPS, (b) SEA, along [100], [110] and [111] directions for the uniform and variable thickness specimens.

5. Conclusions

This work presents a family of elastically-isotropic open-cell variable thickness TPMS shell-lattices with superior stiffness by a strain energy-based optimization algorithm. The cubic symmetry of the shell-lattices is maintained by averaging the sensitivity terms in the optimization process. The optimization results show that all the five selected types of TPMS (N14, OCTO, IWP, FRD, N) shell-lattices are able to achieve elastic isotropy by varying the shell thickness accordingly, among which N14 and OCTO can maintain over 90% of the HS upper bound of bulk modulus. The Young's and shear moduli of all the five types of elastically-isotropic shell-lattices reach 50% ~ 60% and 40% ~ 60% of the HS upper bounds in low relative densities, which significantly outperform elastically-isotropic truss-lattices of equal relative density. Compared with the closed-cell elastically-isotropic plate-lattices, the stiffness properties of the elastically-isotropic shell-lattices are lower, as a trade-off induced by the open-cell topology. The maximum elastic properties achievable by open-cell lattices remain an open question for future research.

The uniform and variable thickness N14 shell-lattices along [100], [110] and [111] directions are fabricated by micro-LPBF with SS316L and tested to verify the stiffness properties. The experimental results are in reasonable agreement with the FEA results. Comparisons of the tested Young's moduli along (1), (2), (6) and (7) directions reveal nearly elastic isotropy between [100] and [110] directions for the variable thickness specimens, with the moduli ratio reduced from 1.08 (uniform) to 1.02 (variable). Although the overall anisotropy in stiffness is still observed due to the anisotropy of the AM fabricated material, the elastic anisotropy is shown to be reduced by varying the shell thickness accordingly. The following large strain compression tests reveal a

layer-by-layer plastic buckling failure mode along [100] direction, while the failures along [110] and [111] directions are related to the shear deformation. It is also shown that the variable thickness specimens possess a reduced anisotropy of plateau stresses and nearly achieve isotropic energy absorption capacity.

In the experimental tests, the constituent material's anisotropy is observed, which induces anisotropy to the macroscopic stiffness properties of the variable thickness designs. A better way to take the anisotropy of the constituent material into consideration is to assume the constituent material to be orthotropic or transversely isotropic, instead of isotropic. Combination of this assumption with the whole analysis and optimization workflow in this work poses a potential opportunity to achieve a family of manufacturable elastically-isotropic open-cell shell-lattices and will be explored in detail in our future work.

Declaration of Competing Interest

The authors declare that they have no known competing financial interests or personal relationships that could have appeared to influence the work reported in this paper.

Acknowledgements

This work is supported by the Innovation and Technology Fund of the Government of the Hong Kong Special Administrative Region (Project No. ITS/008/19).

Appendix

The sensitivity of the optimization problem (11) is derived as:

$$\frac{\partial J}{\partial \delta_i} = \frac{2(\xi-1)}{(c_{11}-c_{12})^2} \left[\frac{\partial c_{44}}{\partial \delta_i} (c_{11}-c_{12}) - c_{44} \left(\frac{\partial c_{11}}{\partial \delta_i} - \frac{\partial c_{12}}{\partial \delta_i} \right) \right], \quad (i=1,2,\dots,N) \quad (\text{A1})$$

with the derivative terms $\frac{\partial c_{11}}{\partial \delta_i}$, $\frac{\partial c_{12}}{\partial \delta_i}$ and $\frac{\partial c_{44}}{\partial \delta_i}$ derived from Eq. (9a) ~ (9c) as:

$$\frac{\partial c_{11}}{\partial \delta_i} = \frac{2}{V} \frac{\partial e^{(U)}}{\partial \delta_i}, \quad (\text{A2a})$$

$$\frac{\partial c_{12}}{\partial \delta_i} = \frac{1}{V} \left[\frac{1}{3} \frac{\partial e^{(T)}}{\partial \delta_i} - \frac{\partial e^{(U)}}{\partial \delta_i} \right], \quad (\text{A2b})$$

$$\frac{\partial c_{44}}{\partial \delta_i} = \frac{2}{V} \frac{\partial e^{(S)}}{\partial \delta_i}, \quad (\text{A2c})$$

The derivatives of the strain energies in Eq. (A2a) ~ (A2c) are derived as [45]:

$$\frac{\partial e^{(j)}}{\partial \delta_i} = \frac{1}{2} [\mathbf{U}_i^{(j)}]^T \frac{\partial \mathbf{K}_i}{\partial \delta_i} \mathbf{U}_i^{(j)} = \frac{1}{2} \left\{ [\mathbf{U}_{i(j)}^{(m)}]^T \frac{\partial \mathbf{K}_i^{(m)}}{\partial \delta_i} \mathbf{U}_{i(j)}^{(m)} + [\mathbf{U}_{i(j)}^{(b)}]^T \frac{\partial \mathbf{K}_i^{(b)}}{\partial \delta_i} \mathbf{U}_{i(j)}^{(b)} \right\}, \quad (i=1,2,\dots,N; \quad j=U,T,S) \quad (\text{A3})$$

where \mathbf{U}_i and \mathbf{K}_i denote the element displacement vector and element stiffness matrix, respectively. Eq. (A3) reveals that $\frac{\partial e^{(j)}}{\partial \delta_i}$ can be decomposed into two parts, i.e., the membrane term and bending term, in which $\mathbf{U}_i^{(m)}$ and $\mathbf{U}_i^{(b)}$ denote the re-organized element membrane displacement vector and element bending displacement vector, while $\mathbf{K}_i^{(m)}$ and $\mathbf{K}_i^{(b)}$ denote the re-organized element membrane stiffness matrix and element bending stiffness matrix. The element membrane stiffness matrix is derived as:

$$\mathbf{K}_i^{(m)} = \int_{A_i} [\mathbf{B}^{(m)}]^T \mathbf{D}^{(m)} \mathbf{B}^{(m)} dA, \\ \mathbf{D}^{(m)} = \frac{E_s \delta_i}{1 - \nu_s^2} \begin{pmatrix} 1 & \nu_s & 0 \\ \nu_s & 1 & 0 \\ 0 & 0 & \frac{1-\nu_s}{2} \end{pmatrix} \quad (\text{A4})$$

where $\mathbf{B}^{(m)}$ denotes the membrane strain-displacement matrix, while δ_i and A_i denote the thickness and mid-surface area of element i . The element bending stiffness matrix is derived from the Kirchhoff-Love plate/shell theory as:

$$\mathbf{K}_i^{(b)} = \int_{A_i} [\mathbf{B}^{(b)}]^T \mathbf{D}^{(b)} \mathbf{B}^{(b)} dA,$$

$$\mathbf{D}^{(b)} = \frac{E_s \delta_i^3}{12(1-\nu_s^2)} \begin{pmatrix} 1 & \nu_s & 0 \\ \nu_s & 1 & 0 \\ 0 & 0 & \frac{1-\nu_s}{2} \end{pmatrix} \quad (A5)$$

where $\mathbf{B}^{(b)}$ denotes the bending strain-displacement matrix. Since both the strain-displacement matrices $\mathbf{B}^{(m)}$ and $\mathbf{B}^{(b)}$ are independent of the shell thickness δ_i , the derivatives of the membrane and bending stiffness matrices in Eq. (A3) are thus obtained as:

$$\frac{\partial \mathbf{K}_i^{(m)}}{\partial \delta_i} = \frac{1}{\delta_i} \mathbf{K}_i^{(m)}, \quad (A6a)$$

$$\frac{\partial \mathbf{K}_i^{(b)}}{\partial \delta_i} = \frac{3}{\delta_i} \mathbf{K}_i^{(b)}, \quad (A6b)$$

The element membrane and bending stiffness matrices $\mathbf{K}_i^{(m)}$ and $\mathbf{K}_i^{(b)}$ are extracted from ABAQUS by adding commands in the .inp file, based on which the derivative terms in Eq. (A3) and (A6a) ~ (A6b) are evaluated. The sensitivity terms are then achieved by Eq. (A1) and (A2a) ~ (A2c).

The derivative of the objective function J with respect to the pseudo-time is derived by the chain rule as:

$$\dot{J} = \sum_{i=1}^N \frac{\partial J}{\partial \delta_i} \dot{\delta}_i, \quad (A7)$$

In this work, the steepest descent method is adopted as the optimizer, meaning $\dot{\delta}_i$ is taken as:

$$\dot{\delta}_i = -\frac{\partial J}{\partial \delta_i}, \quad (i=1, 2, \dots, N) \quad (A8)$$

so that $\dot{J} = -\sum_{i=1}^N \left(\frac{\partial J}{\partial \delta_i} \right)^2 \leq 0$. The element thickness δ_i is then updated by:

$$\delta_i(a+1) = \delta_i(a) + dt \cdot \dot{\delta}_i(a), \quad (i=1, 2, \dots, N) \quad (A9)$$

where the superscript (a) denotes the iteration step, while dt denotes the step size.

References

- [1] L.J. Gibson, Cellular solids, *MRS Bull.* 28(4) (2003) 270-274.
- [2] T. Bückmann, N. Stenger, M. Kadic, J. Kaschke, A. Frölich, T. Kennerknecht, C. Eberl, M. Thiel, M. Wegener, Tailored 3D mechanical metamaterials made by dip-in direct-laser-writing optical lithography, *Adv. Mater.* 24(20) (2012) 2710-2714.
- [3] Z.G. Nicolaou, A.E. Motter, Mechanical metamaterials with negative compressibility transitions, *Nat. Mater.* 11(7) (2012) 608-613.
- [4] M. Kadic, T. Bückmann, N. Stenger, M. Thiel, M. Wegener, On the practicability of pentamode mechanical metamaterials, *Appl. Phys. Lett.* 100(19) (2012) 191901.
- [5] H.N. Wadley, Multifunctional periodic cellular metals, *Philos. Trans. Royal Soc. A* 364(1838) (2006) 31-68.
- [6] M. Rashed, M. Ashraf, R. Mines, P.J. Hazell, Metallic microlattice materials: A current state of the art on manufacturing, mechanical properties and applications, *Mater. Des.* 95 (2016) 518-533.
- [7] Y. Wang, L. Zhang, S. Daynes, H. Zhang, S. Feih, M.Y. Wang, Design of graded lattice structure with optimized mesostructures for additive manufacturing, *Mater. Des.* 142 (2018) 114-123.
- [8] J.B. Ostos, R. Rinaldi, C. m Hammetter, G. Stucky, F. Zok, A. Jacobsen, Deformation stabilization of lattice structures via foam addition, *Acta Mater.* 60(19) (2012) 6476-6485.
- [9] V.S. Deshpande, N.A. Fleck, M.F. Ashby, Effective properties of the octet-truss lattice material, *J. Mech. Phys. Solids* 49(8) (2001) 1747-1769.
- [10] T. Tancogne-Dejean, A.B. Spierings, D. Mohr, Additively-manufactured metallic micro-lattice materials for high specific energy absorption under static and dynamic loading, *Acta Mater.* 116 (2016) 14-28.
- [11] R.M. Lattice, R.X. Rodriguez, L.R. Holmes Jr, F.W. Zok, Effects of nodal fillets and external boundaries on compressive response of an octet truss, *Acta Mater.* 149 (2018) 78-87.
- [12] R. Christensen, Mechanics of low density materials, *J. Mech. Phys. Solids* 34(6) (1986) 563-578.
- [13] N. Francois, T. Arnoux, L. Garcia, S. Hyde, V. Robins, M. Saadatfar, M. Saba, T. Senden, Experimental investigation of the mechanical stiffness of periodic framework-patterned elastomers, *Philos. Trans. Royal Soc. A* 372(2008) (2014) 20120035.
- [14] T. Tancogne-Dejean, D. Mohr, Elastically-isotropic truss lattice materials of reduced plastic anisotropy, *Int. J. Solids Struct.* 138 (2018) 24-39.
- [15] J.B. Berger, H. Wadley, R. McMeeking, Mechanical metamaterials at the theoretical limit of isotropic elastic stiffness, *Nature* 543(7646) (2017) 533-537.
- [16] T. Tancogne-Dejean, M. Diamantopoulou, M.B. Gorji, C. Bonatti, D. Mohr, 3D Plate-Lattices: An Emerging Class of Low-Density Metamaterial Exhibiting Optimal Isotropic Stiffness, *Adv. Mater.* 30(45) (2018) 1803334.
- [17] C. Crook, J. Bauer, A.G. Izard, C.S. de Oliveira, J.M.d.S. e Silva, J.B. Berger, L. Valdevit, Plate-nanolattices at the theoretical limit of stiffness and strength, *Nat. Commun.* 11(1) (2020) 1-11.
- [18] S. Duan, W. Wen, D. Fang, Additively-manufactured anisotropic and isotropic 3D plate-lattice materials for enhanced mechanical performance: Simulations & experiments, *Acta Mater.* 199 (2020) 397-412.

[19] L. Valdevit, A. Pantano, H.A. Stone, A.G. Evans, Optimal active cooling performance of metallic sandwich panels with prismatic cores, *Int. J. Heat Mass Transf.* 49(21-22) (2006) 3819-3830.

[20] S. Baudis, F. Nehl, S.C. Ligon, A. Nigisch, H. Bergmeister, D. Bernhard, J. Stampfl, R. Liska, Elastomeric degradable biomaterials by photopolymerization-based CAD-CAM for vascular tissue engineering, *Biomed. Mater.* 6(5) (2011) 055003.

[21] S.C. Kapfer, S.T. Hyde, K. Mecke, C.H. Arns, G.E. Schröder-Turk, Minimal surface scaffold designs for tissue engineering, *Biomaterials* 32(29) (2011) 6875-6882.

[22] J. Song, Y. Chen, K. Cao, Y. Lu, J.H. Xin, X. Tao, Fully controllable design and fabrication of three-dimensional lattice supercapacitors, *ACS Appl. Mater. Interfaces* 10(46) (2018) 39839-39850.

[23] L. Gao, J. Song, J.U. Surjadi, K. Cao, Y. Han, D. Sun, X. Tao, Y. Lu, Graphene-bridged multifunctional flexible fiber supercapacitor with high energy density, *ACS Appl. Mater. Interfaces* 10(34) (2018) 28597-28607.

[24] J. Xue, L. Gao, X. Hu, K. Cao, W. Zhou, W. Wang, Y. Lu, Stereolithographic 3D printing-based hierarchically cellular lattices for high-performance quasi-solid supercapacitor, *Nanomicro Lett.* 11(1) (2019) 1-13.

[25] A.H. Schoen, Infinite periodic minimal surfaces without self-intersections, *National Aeronautics and Space Administration* 1970.

[26] C. Bonatti, D. Mohr, Mechanical performance of additively-manufactured anisotropic and isotropic smooth shell-lattice materials: Simulations & experiments, *J. Mech. Phys. Solids* 122 (2019) 1-26.

[27] Z. Chen, Y.M. Xie, X. Wu, Z. Wang, Q. Li, S. Zhou, On hybrid cellular materials based on triply periodic minimal surfaces with extreme mechanical properties, *Mater. Des.* 183 (2019) 108109.

[28] L. Zhang, S. Feih, S. Daynes, S. Chang, M.Y. Wang, J. Wei, W.F. Lu, Energy absorption characteristics of metallic triply periodic minimal surface sheet structures under compressive loading, *Addit. Manuf.* 23 (2018) 505-515.

[29] F. Bobbert, K. Lietaert, A.A. Eftekhari, B. Pouran, S. Ahmadi, H. Weinans, A.A. Zadpoor, Additively manufactured metallic porous biomaterials based on minimal surfaces: A unique combination of topological, mechanical, and mass transport properties, *Acta Biomater.* 53 (2017) 572-584.

[30] S.J. Callens, N. Tümer, A.A. Zadpoor, Hyperbolic origami-inspired folding of triply periodic minimal surface structures, *Appl. Mater. Today* 15 (2019) 453-461.

[31] D.J. Yoo, Heterogeneous porous scaffold design for tissue engineering using triply periodic minimal surfaces, *Int. J. Precis. Eng. Manuf.* 13(4) (2012) 527-537.

[32] S. Vijayavenkataraman, L. Zhang, S. Zhang, J.Y. Hsi Fuh, W.F. Lu, Triply periodic minimal surfaces sheet scaffolds for tissue engineering applications: An optimization approach toward biomimetic scaffold design, *ACS Appl. Bio Mater.* 1(2) (2018) 259-269.

[33] C. Bonatti, D. Mohr, Smooth-shell metamaterials of cubic symmetry: Anisotropic elasticity, yield strength and specific energy absorption, *Acta Mater.* 164 (2019) 301-321.

[34] C. Soyarslan, V. Blümer, S. Bargmann, Tunable auxeticity and elastomechanical symmetry in a class of very low density core-shell cubic crystals, *Acta Mater.* 177 (2019) 280-292.

[35] B. Deng, G.J. Cheng, Soap film inspired mechanical metamaterials approaching theoretical bound of stiffness across full density range, *Mater. Horizons* 8(3) (2021) 987-996.

[36] S.J. Callens, C.H. Arns, A. Kuliesh, A.A. Zadpoor, Decoupling minimal surface metamaterial properties through multi-material hyperbolic tilings, *Adv. Funct. Mater.* (2021).

- [37] J.C. Nitsche, *Lectures on minimal surfaces*: vol. 1, Cambridge University Press 1989.
- [38] P.J. Gandy, S. Bardhan, A.L. Mackay, J. Klinowski, Nodal surface approximations to the P, G, D and I-WP triply periodic minimal surfaces, *Chem. Phys. Lett.* 336(3-4) (2001) 187-195.
- [39] K.A. Brakke, *The Surface Evolver*, *Exp. Math.* 1(2) (1992) 141-165.
- [40] D.W. Lee, K.A. Khan, R.K.A. Al-Rub, Stiffness and yield strength of architectured foams based on the Schwarz Primitive triply periodic minimal surface, *Int. J. Plast.* 95 (2017) 1-20.
- [41] B.D. Nguyen, S.C. Han, Y.C. Jung, K. Kang, Design of the P-surfaced shellular, an ultra-low density material with micro-architecture, *Comput. Mater. Sci.* 139 (2017) 162-178.
- [42] S.L. Omairey, P.D. Dunning, S. Sriramula, Development of an ABAQUS plugin tool for periodic RVE homogenisation, *Eng. Comput.* 35(2) (2019) 567-577.
- [43] Mechanical testing of metals — Ductility testing — Compression test for porous and cellular metals, ISO 13314:2011, International Organization for Standardization, 2011.
- [44] Q.M. Li, I. Magkiriadis, J.J. Harrigan, Compressive strain at the onset of densification of cellular solids, *J. Cell. Plast.* 42(5) (2006) 371-392.
- [45] W. Zhang, G. Dai, F. Wang, S. Sun, H. Bassir, Using strain energy-based prediction of effective elastic properties in topology optimization of material microstructures, *Acta Mech. Sin.* 23(1) (2007) 77-89.